







Cite this: *Nanoscale*, 2018, **10**, 9097

## Platinum nanoparticles: a non-toxic, effective and thermally stable alternative plasmonic material for cancer therapy and bioengineering†

Akbar Samadi,  ‡<sup>a</sup> Henrik Klingberg, ‡<sup>a</sup> Liselotte Jauffred,<sup>a</sup> Andreas Kjær, <sup>b</sup> Poul Martin Bendix <sup>a</sup> and Lene B. Oddershede \*<sup>a</sup>

Absorption of near infrared (NIR) light by metallic nanoparticles can cause extreme heating and is of interest for instance in cancer treatment since NIR light has a relatively large penetration depth into biological tissue. Here, we quantify the extraordinary thermoplasmonic properties of platinum nanoparticles and demonstrate their efficiency in photothermal cancer therapy. Although platinum nanoparticles are extensively used for catalysis, they are much overlooked in a biological context. Via direct measurements based on a biological matrix we show that individual irradiated platinum nanoparticles with diameters of 50–70 nm can easily reach surface temperatures up to 900 K. In contrast to gold nanoshells, which are often used for photothermal purposes, we demonstrate that the platinum particles remain stable at these extreme temperatures. The experiments are paralleled by finite element modeling confirming the experimental results and establishing a theoretical understanding of the particles' thermoplasmonic properties. At extreme temperatures it is likely that a vapor layer will form around the plasmonic particle, and we show this scenario to be consistent with direct measurements and simulations. Viability studies demonstrate that platinum nanoparticles themselves are non-toxic at therapeutically relevant concentrations, however, upon laser irradiation we show that they efficiently kill human cancer cells. Therefore, platinum nanoparticles are highly promising candidates for thermoplasmonic applications in the life sciences, in nano-medicine, and for bio-medical engineering.

Received 19th March 2018,

Accepted 21st April 2018

DOI: 10.1039/c8nr02275e

rsc.li/nanoscale

## 1 Introduction

The photothermal properties of metallic nanoparticles are uniquely distinct from those of the similar bulk material. At resonance between the incoming electromagnetic wave and the electron oscillations, the absorption is significantly increased.<sup>1–3</sup> The absorbed energy is dissipated as heat from the metallic nanoparticle, which thereby functions as an efficient thermoplasmonic light-to-heat converter.<sup>2,4</sup>

The extreme thermoplasmonic properties of metallic nanoparticles make them highly desirable as nano-heaters for several purposes, for instance for diagnosis, therapies and surgery.<sup>5</sup> One important application is for cancer therapy,

where irradiated gold nanoshells (AuNSs) and gold nanospheres have been shown to effectively reduce the size of tumors in living animals.<sup>6–9</sup> Current efforts focus on development of NIR resonant plasmonic nanoparticles with sizes optimized for systemic administration *via* the enhanced permeability and retention (EPR) effect,<sup>10,11</sup> which is optimal for particles with diameter around 50 nm.<sup>12</sup> Additionally, the particles should be: (i) non-toxic, (ii) stable under physiological conditions before, during and after irradiation, and (iii) producible in large scale quantities at high quality. Several NIR resonant nanoparticles have been designed, for instance gold nanorods, nano-matryoshkas,<sup>13</sup> and gold nanoshells (AuNSs).<sup>14</sup> Each of these particle types have their pros and cons and it is challenging to pinpoint a particle type that passes all criteria.

Plasmonic nanoparticles have potential for numerous other applications in the life sciences, *e.g.*, for laser activated delivery of molecules carried by metallic nanoparticles<sup>15–17</sup> or for selective cell- or vesicle fusion.<sup>18,19</sup> Nanoparticles, especially those made of platinum, are also widely used for catalytic purposes<sup>20</sup> where the catalytic properties of platinum nanoparticles crucially depend on the particle's size and shape.<sup>21</sup> Namely for

<sup>a</sup>Niels Bohr institute, University of Copenhagen, Blegdamsvej 17, 2100 Copenhagen, Denmark. E-mail: oddershede@nbi.ku.dk

<sup>b</sup>Dept. of Clinical Physiology, Nuclear Medicine & PET and Cluster for Molecular Imaging, Dept. of Biomedical Sciences, Rigshospitalet & University of Copenhagen, Denmark Blegdamsvej 3, 2200 Copenhagen, Denmark

†Electronic supplementary information (ESI) available. See DOI: 10.1039/C8NR02275E

‡These authors contributed equally and are joint first authors.

industrial applications, such as catalysis, it is important that the particles are thermally stable and do not restructure upon heating to high temperatures.<sup>22</sup> Other areas of application include optical trapping<sup>23–25</sup> and enhancement of spectroscopic signals<sup>26</sup> by plasmonic nanoparticles which further emphasizes their diverse applicability in science.

This work is motivated by the wide-spread use of plasmonic nanoparticles and by the fact that most focus has been on gold and remarkable little attention has been on alternative plasmonic materials which may possess equally good or better thermal stability and photothermal efficiency.<sup>27,28</sup> Here, we report on the extraordinary plasmonic properties and stability of NIR irradiated spherical platinum nanoparticles (PtNPs). The photothermal efficiency and stability of PtNPs are experimentally and theoretically compared to 150 nm NIR resonant AuNS, which are currently used for thermoplasmonic therapy, and to massive gold nanoparticles. To demonstrate the extreme thermoplasmonic efficiency of PtNPs, we used them to photothermally kill human ovarian cancer cells while also proving that the non-irradiated PtNPs are non-toxic. Compared to similar particles, the PtNPs with sizes optimal for cellular uptake and EPR delivery, thereby fulfilling conditions (i)–(iii) above, are found to be extremely efficient and thermally stable light-to-heat converters and are promising candidates for NIR based bioengineering purposes and thermoplasmonic applications.

## 2 Experimental

### 2.1 Simulations

To simulate the temperature profile around irradiated nanoparticles, we performed finite element modeling using the FEM Multiphysics package from COMSOL (Stockholm, Sweden) taking into account, *e.g.*, the thermal conductivity at the water/glass interface and the focal intensity distribution of light. For this, we formulated the heat generation per unit volume, Maxwell's equations were solved for the electrical field, and the temperature profile was found *via* the Poisson equation, details on the modeling can be found in ESI† and in Ma *et al.* and Govorov *et al.*<sup>29,30</sup> The temperature increase at the surface of a nanoparticle was calculated using the following time-dependent heat transfer equation:<sup>29–32</sup>

$$\rho(\mathbf{r})C_p(\mathbf{r})\frac{\partial T(\mathbf{r})}{\partial t} - \nabla \cdot [k(\mathbf{r})\nabla T(\mathbf{r})] = Q. \quad (1)$$

Here,  $\rho(\mathbf{r})$  and  $C_p(\mathbf{r})$  are the position dependent density and specific heat capacity, respectively, at constant pressure.  $T(\mathbf{r})$  is the absolute temperature,  $k(\mathbf{r})$  is the thermal conductivity and  $Q$  is the generated heat,  $Q = J \cdot E = C_{\text{abs}}I$ , where  $J$  is the current density,  $E$  is the electrical field,  $C_{\text{abs}}$  is the absorption cross section of nanoparticle and  $I$  is the intensity of the irradiating laser. Modeling of eqn (1) revealed that the temperature reaches a steady-state value  $\sim 100$  ns after irradiation (see Fig. S1†), which is consistent with previously reported time scales.<sup>32</sup>

### 2.2 Materials

The nanoparticles used in this study were NanoXact 30 nm platinum nanoparticles (PtNPs), NanoXact 50 nm PtNPs, NanoXact 70 nm PtNPs (citrate surface) and 150 nm gold nanoshells (AuNSs) with peak absorbance at 800 nm (lipoic acid surface) (nanoComposix, San Diego, CA, USA). All other chemicals were purchased from Sigma-Aldrich (St Louis, MO, USA) if nothing else is specified.

### 2.3 Single nanoparticle temperature measurements

A lipid bilayer based temperature sensing assay was prepared by fusion of small lipid vesicles to an ultra clean hydrophilic glass substrate, further details can be found in ref. 9, 29 and 33.

**2.3.1 Bilayer formation and single particle heating.** Briefly,  $2 \times 10^{-6}$  moles of saturated lipids 1,2-dipentadecanoyl-*sn*-glycero-3-phosphocholine (DC<sub>15</sub>PC, Avanti Polar Lipids Inc., Alabaster, AL, USA) were mixed with  $2 \times 10^{-8}$  moles (1 mol%) of 3,3'-dilinoleylloxycarbonyl perchlorate (FAST-DiO™) (Molecular Probes, Eugene, OR, USA) fluorophores in chloroform. The chloroform was evaporated under nitrogen flow and dried in vacuum for 2 hours. 150 mM NaCl in PBS buffer (Gibco, NY, USA) was added to hydrate the lipid film and left for 1 hour at 37 °C. Small lipid vesicles were formed by extrusion through a polycarbonate filter with pore size of 50 nm. A hydrophilic glass substrate which had been plasma cleaned (PDC-002, Harrick Plasma, Ithaca, NY, USA) for 30 min in oxygen was used. The solution containing PtNPs or AuNSs, diluted in milliQ water, was added to the glass surface and the nanoparticles were allowed to adhere to the glass. The surface was dried with nitrogen and subsequently a volume of 200  $\mu$ l of the extruded unilamellar vesicles was added to the glass surface and allowed to fuse with the glass surface for 2 hours at 37 °C. The surface was rinsed thoroughly using milliQ water preheated to  $\sim 50$  °C.

**2.3.2 Optical setup.** Confocal imaging of the fluorescent lipid bilayer was carried out on a Leica TCS SP5 II confocal microscope (Leica Microsystems, Wetzlar, Germany) equipped with optical tweezers and a piezoelectric stage which allowed precise positioning of the NPs inside the laser focus as sketched in Fig. 2a, details of the setup can be found in the ESI† and in Richardson *et al.*<sup>34</sup> The optical trap based on a 1064 nm tightly focused Gaussian beam was used to heat the NPs. The NIR and imaging laser beams were focused by a  $63 \times 1.2$  NA, HC PL APO Leica objective. The NPs were imaged in reflection mode by  $\lambda = 633$  nm laser light. FAST-DiO was excited by  $\lambda = 488$  nm and emission collected with a bandwidth from 500 nm to 551 nm. The sample was kept on a temperature controlled stage and the sample temperature was measured to be  $T_{\text{ambient}} = 28$  °C which was used in the calculations of nanoparticle temperatures.

**2.3.3 Image analysis.** Individual melting footprints centered around the nanoparticles were analyzed using Matlab (The MathWorks, Inc., Natick, Massachusetts). The melting radius ( $r_m$ ) equals the distance from the particle center to the

location of the melting transition where the temperature was  $T_m(r_m) = 33.8$  °C. The fluorescent intensity as a function of distance from the center of the particle was found by averaging the intensity in a circle around the particle.  $r_m$  was determined by setting a threshold,  $T_r$ , below which the fluorescence was identical to the background level. The background level was determined in a region of interest, ROI<sub>bg</sub>, outside the melted region. The threshold,  $T_r$ , was defined as the value at which the intensity had dropped to 50% of the maximum value in a region of interest inside the melted region. To find the temperature at the surface of the particle irradiated with an intensity  $I$  we used the equation:  $\Delta T(D) = \text{constant} \cdot I/D$ ,<sup>33</sup> where  $D$  is the distance from the particle center and the equation is valid for  $R \leq D$  ( $R$  being the radius of the metallic nanoparticle). The constant can be found because at  $D = r_m$  the temperature equals the phase transition temperature.

#### 2.4 Bulk temperature measurements

To measure the temperature of bulk solutions we prepared nanoparticle solutions in disposable cuvettes (Brand GmbH, Wertheim, Germany). To measure the absorbance we used a Cary 5000 UV-Vis-NIR spectrophotometer (Agilent Technologies, Santa Clara, CA, USA) at  $\lambda = 1064$  nm. To obtain a constant optical density of  $\lambda_L = 0.14$  for all nanoparticle solutions, the samples were diluted in Millipore water to the following concentrations: 50 nm PtNPs to a density of  $0.061$  mg ml<sup>-1</sup> (corresponding to a particle concentration of  $4.1 \times 10^{10}$  ml<sup>-1</sup>), 70 nm PtNPs to  $0.050$  mg ml<sup>-1</sup> ( $1.2 \times 10^{10}$  ml<sup>-1</sup>), and AuNSs to  $0.014$  mg ml<sup>-1</sup> ( $0.1 \times 10^{10}$  ml<sup>-1</sup>). We also prepared nanoparticle solutions that were mass density matched to  $0.05$  mg ml<sup>-1</sup>. This mass density matching corresponds to the following particle concentrations:  $3.4 \times 10^{10}$  ml<sup>-1</sup> for 50 nm PtNPs,  $1.2 \times 10^{10}$  ml<sup>-1</sup> for 70 nm PtNPs, and  $0.33 \times 10^{10}$  ml<sup>-1</sup> for the AuNSs. A NIR Nd:YVO4 diode-laser (Spectra Physics, BL106C, Santa Clara, CA, USA) ( $\lambda = 1064$  nm) irradiated the cuvettes containing the nanoparticle solutions. The laser spot was focused to  $\sim 5$  mm in diameter, slightly smaller than the cuvette width. We used an InSb IR camera (FLIR Systems, SC4000, Boston, MA) with a spectral range of 3–5  $\mu\text{m}$  to measure the heating characteristics of the sample. The IR camera was mounted at an angle of approximately 90° to the laser such that the sample was irradiated in an area coinciding with the active area of the camera while not interfering with the imaging. Each sample was irradiated at a constant laser power in the range from 0.5–5 W and the imaging rate of the camera was 4 min<sup>-1</sup>. Prior to each experiment we sonicated and mixed the sample thoroughly to create a uniform distribution of nanoparticles and confirmed the laser power using a standard power meter (P-link; Gentec, Sweden). We selected a region of interest at the cuvette to measure the temperature, using the ThermoVision software (FLIR Systems), more details in the ESI.†

#### 2.5 Platinum nanoparticle toxicity and photothermal cancer therapy

Human ovarian SK-OV-3 cancer cells were cultured in McCoy's 5A medium (Gibco) supplemented with 10% FBS and 1% peni-

cillin and streptomycin (Gibco) under normal cell culture conditions (37 °C, 5% CO<sub>2</sub> and 95% humidity).

**2.5.1 Cellular toxicity.** Cells were seeded ( $2.5 \times 10^4$  cells per cm<sup>2</sup>) on 24-well cell culture plates (Nunclon Delta, Nunc, Thermo Fischer Scientific, Roskilde, DK). One day after seeding SK-OV-3 cells were exposed to 30 nm PtNPs, 50 nm PtNPs and 70 nm PtNPs (0, 0.08, 0.4, 2, 10 and 50  $\mu\text{g ml}^{-1}$ ) in McCoy's 5A medium without phenol red (GE Healthcare Life Sciences, HyClone Laboratories, Logan, UT, USA). After 24 hours of particle exposure, PtNP containing culture medium was aspirated and cells were washed two times in pre-warmed PBS. Then cells were incubated with 500 nM CellROX® Deep Red (Molecular Probes) for 30 minutes (at normal cell culture conditions), cells were then detached using Accutase™ (Gibco) and immediately transferred to a pre-cooled cooling rack (BioCision, San Rafael, CA, USA). Cells were centrifuged and resuspended in annexin-binding buffer (10 mM HEPES, 140 mM NaCl, 2.5 mM CaCl<sub>2</sub>, pH 7.4) with annexin V, Alexa Fluor® 488 conjugate (Molecular Probes) and LIVE/DEAD® Fixable Near-IR Dead Cell Stain (Invitrogen, Carlsbad, CA, USA) both following the manufactures instructions. Flow cytometry was performed with a BD FACS canto II (Becton, Dickinson and Company). Forward scatter (FSC-A) and side scatter (SSC-A) were detected using a blue laser ( $\lambda = 488$  nm) and detection at the same wavelength. The levels of annexin V 488 conjugate was detected using a blue excitation laser ( $\lambda = 488$  nm) and a 530/30 nm emission filter. CellROX and LIVE/DEAD was detected using a red excitation laser ( $\lambda = 633$  nm) and a 660/20 nm emission filter and a 780/60 nm emission filter, respectively. The data was compensated and analyzed using Flowing Software (version 2.5.1, Cell Imaging Core, Turku Centre for Biotechnology). Compensation for spectral overlap between the different fluorophores were performed by using unstained cells and cells stained with only CellRox, annexin V 488 or LIVE/DEAD, respectively.

**2.5.2 Photothermal cancer therapy.** SK-OV-3 cells were seeded on 35 mm Petri dishes with 20 mm glass microwell inserts (MatTek Corporation, Ashland, MA, USA). Cells were exposed to 30 nm PtNPs, 50 nm PtNPs, 70 nm PtNPs ( $50 \mu\text{g ml}^{-1}$ ) for 24 hours as described earlier. Before laser treatment of the cells particle containing medium was removed and, after three times wash with pre-heated PBS, replaced with fresh phenol red free medium. SK-OV-3 cells were treated with an 808 nm laser (ML6600, Modulight, Tampere, Finland) using an illumination kit with a flattop beam profile and a 5 mm diameter of even illumination (maximum variation of mean intensity is 10%). The treatment was performed with a laser intensity of 45 W cm<sup>-2</sup> for 5 minutes. After 24 hours cells were stained with 5  $\mu\text{M}$  calcein AM (Molecular Probes) for 15 minutes and fluorescent imaging was performed with a 10× objective on a Nikon Eclipse Ti microscope (Nikon, Tokyo, Japan) (excitation filter: 490/10, emission filter: 535/45) equipped with a motorized stage. The multiple images of the full area of the glass insert were stitched together using NIS Elements software (Nikon).

**2.5.3 Statistics.** Analysis of variance (ANOVA) was performed using IBM SPSS statistics (version 24.0.0.0) (IBM

Corporation, Armonk, NY, USA). For groups passing Levene's test for homogeneity of variance a Tukey *post-hoc* test was performed, while for groups failing Levene's test a Games-Howell *post-hoc* test was performed. In all cases a significant level of  $P < 0.05$  was applied.

## 3 Results and discussion

### 3.1 Heating and thermal stability of individual irradiated platinum nanoparticles

The heating of an irradiated nanoparticle is directly proportional to its absorption cross section. For PtNPs the theoretically calculated dependence of the absorption cross section on particle size and wavelength is shown in Fig. 1a. The calculated absorption cross sections for AuNSs with a constant core diameter of  $d_c = 120$  nm and with varying shell thickness (from 2.5 nm to 65 nm) are shown in Fig. 1b. Although the AuNSs are relatively large (150 nm in diameter) compared to the PtNPs of this study (30–70 nm in diameter, optimally sized for EPR delivery), a comparison to AuNSs is highly relevant due to the tunability of their resonance peak to the NIR region (see Fig. 1c).

The particles used in the experimental studies are massive PtNPs with diameters of 30 nm, 50 nm and 70 nm and a NIR resonant AuNSs with  $d_c = 120$  nm and a total diameter of 150 nm. The experimentally measured extinction cross sections for these particles as a function of wavelength are given in Fig. 1c. It is clear from Fig. 1 that 150 nm AuNS should heat more than the PtNPs here investigated upon NIR irradiation. Still, however, PtNPs with diameters around 50 nm (optimal for EPR delivery) do have significant absorption in the NIR.

The extinction cross section,  $C_{\text{ext}}$ , is a sum of the absorption,  $C_{\text{abs}}$ , and scattering,  $C_{\text{scat}}$  cross sections. Theoretical calculations of these optical cross sections for Pt30, Pt50, Pt70 and 150 nm AuNS are given in ESI Fig. S2.† Numerical values

at 1064 nm are given in ESI Table S1,† which also contains the values for massive gold nanoparticles (AuNPs) with diameters similar to the investigated PtNPs. From these values it is evident that PtNPs heat significantly more upon NIR irradiation than similarly sized AuNPs. Also, the values of  $C_{\text{abs}}$  confirm that if irradiated by a wavelength of 1064 nm AuNSs are expected to heat significantly more than PtNPs.

We directly measured the temperature of an irradiated PtNP or AuNS *via* a heat-sensitive biological matrix as sketched in Fig. 2a. In short, the irradiated nanoparticles were immobilized on a lipid bilayer kept at a temperature below its phase transition temperature,  $T_m$ , and containing incorporated phase-sensitive fluorophores. Upon irradiation the temperature around the metallic nanoparticle may exceed  $T_m$  and the fluorophores partition into the melted region (as shown in Fig. 2b), thus allowing for quantification of the extent of the melted region and consequently of the entire temperature profile. Details of the procedures are given in the Experimental section and in Bendix *et al.*<sup>33</sup> and Ma *et al.*<sup>29</sup>

By this method, we quantified the heating from single irradiated PtNPs with diameters of 30 nm, 50 nm and 70 nm using laser powers ranging from 0 to 500 mW. This size range is particularly interesting as it coincides with the optimal for cellular uptake.<sup>12</sup> Results from a typical experiment are shown in Fig. 2c, where the white symbols show the measured temperature profile surrounding an irradiated 70 nm PtNP. Within the error-bars (denoting one standard deviation), the experimental results are consistent with the simulated values (full red line). The calculated temperatures as a function of distance to the Pt70 particle are also shown by the background colors.

The radius of the melted area scales linearly with laser power, examples at 85 mW, 196 mW and 315 mW are shown in Fig. 2b. Average values of the radii of the melted regions as a function of laser power are shown in Fig. 2d and f for Pt70 and Pt50, respectively, and the corresponding temperature at the

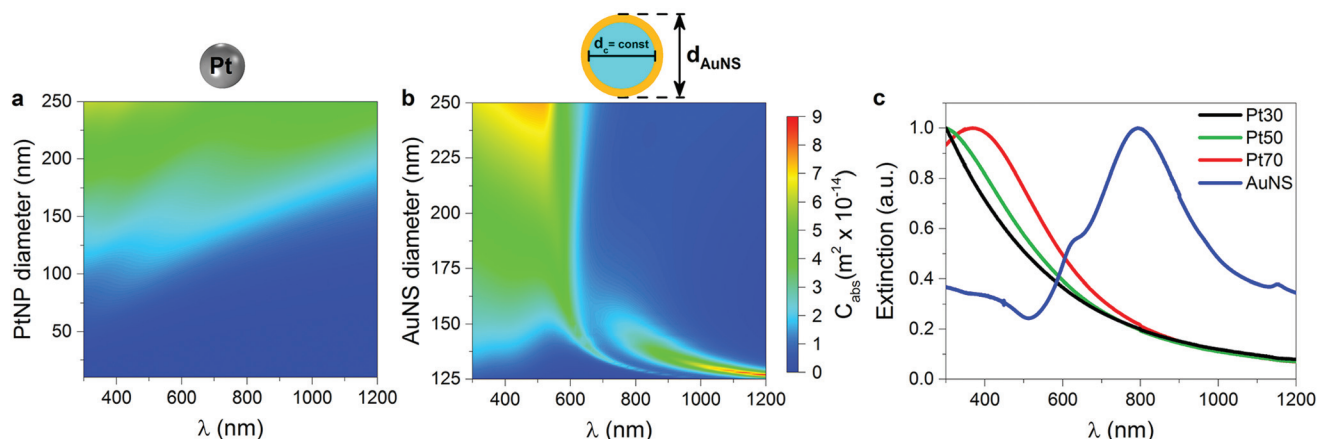


**Fig. 1** Absorption of light by nanoparticles. (a) The absorption cross section calculated by finite element modeling as a function of particle size and wavelength of the irradiating light for platinum nanoparticles (PtNPs). (b) As (a) but for gold nanoshells (AuNSs) with a silica core with constant diameter ( $d_c = 120$  nm) and varying gold shell thickness ( $2.5 \text{ nm} < t_{\text{Au}} < 65 \text{ nm}$ ). The total AuNS diameter,  $d_{\text{AuNS}} = d_c + 2t_{\text{Au}}$ , is hence varied in the interval between 125 nm and 250 nm. (c) Experimentally measured extinction cross sections of PtNPs with diameters 30 nm, 50 nm, and 70 nm and AuNSs with  $d_{\text{AuNS}} = 150$  nm and  $t_{\text{Au}} = 15$  nm.

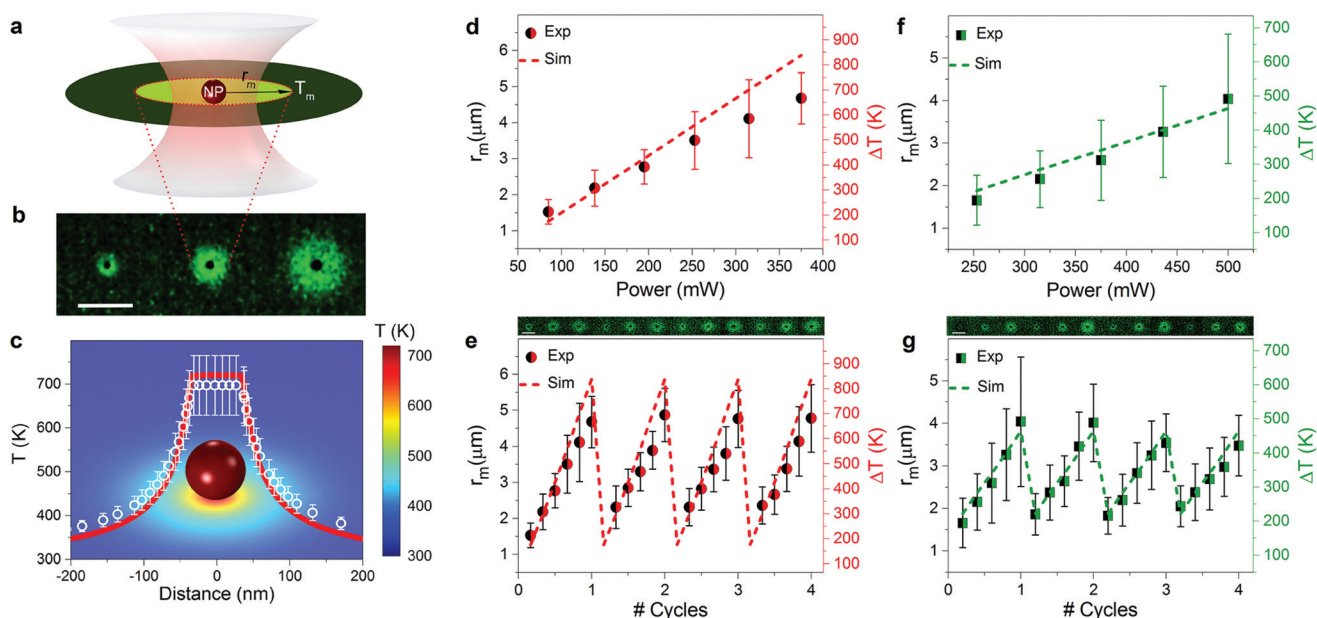


**Fig. 2** Quantification of heating and thermal stability of individual irradiated platinum nanoparticles (PtNPs). (a) Illustration (not to scale) of the setup for direct experimental measurements of the heating of irradiated nanoparticles. A tightly focused 1064 nm laser (red cone) irradiates a nanoparticle immobilized onto a glass coverslip. The coverslip is coated with a lipid bilayer (dark green) incorporating phase-sensitive fluorophores which partition into the melted area (light green).  $r_m$  denotes the radius of the melted area around the heated nanoparticle and  $T_m$  is the phase transition temperature. (b) Representative examples of confocal images showing the partitioning of phase sensitive fluorophores into the melted area around an irradiated 70 nm PtNP. The laser powers used are 85 mW, 195 mW and 315 mW, respectively, going from left to right. The scale bar is 10  $\mu\text{m}$ . (c) Temperature profile around a 70 nm PtNP irradiated by a 1064 nm laser with 195 mW. The white symbols show the experimentally determined temperature profile (an average of  $n = 7$  experiments) and the red solid line shows the temperature profile predicted by the finite element modeling. (d), (f) Symbols show the experimentally measured melted radius (left axes) and corresponding surface temperature change (right axes) for individual irradiated PtNPs with diameters of 70 nm (red, d) and 50 nm (green, f), respectively, as a function of laser power. The dashed lines show the corresponding finite element modeling (FEM) predictions. (e), (g) Symbols show the experimentally measured melted radius (left axes) and corresponding surface temperature increase (right axes) for individual irradiated PtNPs with diameters of 70 nm (red, e) and 50 nm (green, g), respectively, during repeated heating cycles. Each cycle has laser powers as depicted in (d) and (f). The dashed lines show the corresponding FEM predictions. The upper panels show representative and corresponding confocal images of the experiments, the scale bar is 10  $\mu\text{m}$ . Each data point denotes measurements on at least  $n = 7$  different nanoparticles and the error bars denote one standard deviation.

surface of the irradiated nanoparticle is given by the right axes. Irradiated PtNPs undergo temperature increases up to  $\sim 700$  K (at 375 mW) and  $\sim 500$  K (at 500 mW) for 70 nm and 50 nm PtNPs, respectively. These temperatures are significantly higher than previously observed for laser irradiated smaller PtNPs (1–21 nm).<sup>35</sup> We find that the temperature increase for 70 nm ( $\sim 700$  °C at 375 mW) and 50 nm PtNPs ( $\sim 300$  °C at 375 mW) fit the theoretically expected values, since the volume of 70 nm PtNPs is  $\sim 2.5$  times larger than 50 nm PtNPs. At laser powers above 375 mW the lipid layer surrounding a 70 nm PtNP was destroyed as evident from an irreversible destruction of the fluorescence in proximity of the nanoparticle. The 30 nm PtNPs, however, did not heat enough to melt the surrounding lipid bilayer for laser powers between 0 and 500 mW; this is consistent with the low  $C_{\text{abs}}$  of Pt30 at 1064 nm (see ESI Table S1†).

To investigate whether the PtNPs could sustain such high temperatures without restructuring, we exposed the particles to repeated heating cycles. The temperature increase *versus* laser power was reproducible in at least four consecutive cycles in which the 70 nm and 50 nm PtNPs reached maximum

temperature changes of  $\sim 700$  K and  $\sim 500$  K, respectively, as shown in Fig. 2e and g. This demonstrates an extreme thermal stability of spherical PtNPs. The upper panels in Fig. 2e and g display three representative confocal images from each cycle. The reproducibility of the consecutive cycles confirms that the PtNPs are thermally stable, at least up to absolute temperatures of 720 °C. This maximum temperature under 1064 nm NIR irradiation is quite extreme, especially considering the fact that the absorption cross sections of the 70 nm and 50 nm PtNPs peaks around 300–400 nm and the particles were thereby irradiated off-resonance at a wavelength of 1064 nm.

The dashed lines in Fig. 2d and f show the expected temperature increase at the surface of the irradiated particles in water and adhered to a glass substrate as obtained by FEM. As visible from these graphs, the calculated increase in surface temperature agrees well with the experimental measurements. Hence, the extreme heating of irradiated PtNPs can be explained from the material properties of platinum and the reproducibility in the heating cycles (shown in Fig. 2e and g) strongly indicates that PtNPs retain an intact structural integrity within the entire measured temperature range.

### 3.2 Possible formation of a vapor layer around the irradiated particle

In literature it has been suggested, but never directly experimentally proven, that extensive heating of metallic nanoparticles may cause the formation of a vapor layer around the nanoparticle. The local boiling temperature around an irradiated nanoparticle depends on the pressure within a nanoscale bubble<sup>36</sup> and on the surface curvature of the nanoparticle.<sup>37</sup> Hence, the critical water boiling temperature is expected to be much higher than 100 °C around a metallic nanoparticle. If a vapor layer is formed, it would act as an insulator and quickly accelerate the heating of the nanoparticle which could then undergo a gradual structural change or even fragment.

To test the possibility of vapor layer formation around irradiated PtNPs we used FEM to calculate the expected temperature increase if a 20 nm vapor layer is formed around an irradiated PtNP. The higher the temperature, the more likely formation of a vapor layer. Therefore, for this simulation we used a 70 nm PtNP irradiated by 375 mW, the maximum laser power used to irradiate Pt70 in the experiments, results are shown in Fig. 3. It is realistic that PtNPs at such elevated temperatures melt the glass substrate locally and become partly embedded, as has previously been shown to occur for irradiated gold nanoparticles.<sup>38,39</sup> For this reason, three scenarios were simulated: (i) no vapor layer is formed around the PtNP which is resting on the glass substrate (see Fig. 3a, d and g). (ii) The PtNP is encapsulated by a vapor layer and is resting onto the glass substrate (see Fig. 3b, e and h). (iii) The heated PtNP has melted the adjacent glass substrate and has become half-way embedded into the glass substrate with a vapor layer separating the particle from the fluid (see Fig. 3c, f and i). In situation (i), with no vapor layer formed, the absolute temperature reached during irradiation by 375 mW is  $\sim 1076$  K ( $\sim 804$  °C). In situation (ii), where the particle is surrounded by a vapor shell just touching the surface, the expected absolute temperature is  $\sim 2200$  K ( $\sim 1928$  °C). In situation (iii), where the particle is partially embedded into the substrate, the expected absolute temperature is  $\sim 1128$  K ( $\sim 856$  °C). In the direct experimental measurements, we obtained an absolute temperature of  $\sim 700$  °C, which is reasonably consistent with scenarios (i) and (iii). Hence, at current we cannot firmly rule out or confirm the presence of a vapor layer around irradiated and substantially heated PtNPs. However, scenario (ii), where a vapor layer formed without the particle embedding into the glass substrate, seems unlikely.

### 3.3 Heating and thermal stability of individual AuNS

Due to their strong absorption in the NIR, AuNSs are among the most promising candidates for photothermal cancer therapy and have been approved by the American food and drug administration (FDA) for clinical use. Little is known, however, about the thermal stability of AuNSs at high temperatures. The surface plasmon resonance peak of 150 nm AuNSs (silica core diameter  $\sim 120$  nm, gold shell thickness  $\sim 15$  nm) is

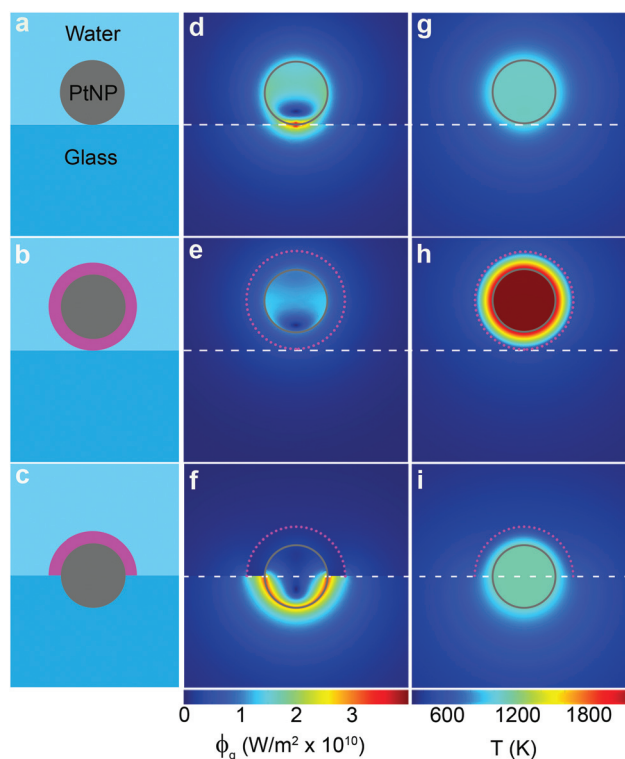


**Fig. 3** Effect of vapor shell formation around an irradiated 70 nm platinum nanoparticle (PtNP). The figure shows three different possible scenarios for an irradiated 70 nm PtNP and the consequences for its temperature profile. The laser power used for the simulations was 375 mW and the depicted temperatures are from a steady-state situation. (a) In the first scenario the PtNP is located in an aqueous environment on top of a glass coverslip, no vapor shell is formed. (b) In the second scenario a 20 nm vapor layer has formed around the irradiated PtNP which is located on top of a glass coverslip. (c) In the third scenario the irradiated PtNP is half-way embedded into the glass coverslip and a half-shell of vapor is formed between the particle and the water. (d–f) The magnitude of the conductive heat flux ( $\phi_q$ ) calculated by FEM for the scenarios depicted in (a), (b), and c, respectively. (g–i) FEM calculated temperature profiles, ( $T$ (K)), around the irradiated PtNP in of scenarios (a), (b), and (c), respectively.

around 800 nm (see Fig. 1c). The absorption cross section of AuNSs at 1064 nm is approximately a factor of 20 and 6 times higher than that of 50 nm and 70 nm PtNPs, respectively (numerical values of optical cross sections are given in Table S1†). Hence, the expected temperature increase around an irradiated 150 nm AuNS is significantly higher than that of 50 nm or 70 nm PtNPs, Fig. S3† shows a direct comparison of the expected temperature profiles at 85 mW.

Using the bilayer assay, we experimentally quantified the heating of irradiated individual 150 nm AuNSs. The radii of the melted areas around individual irradiated AuNSs are shown in Fig. 4a (left axis) for increasing laser powers. The corresponding temperatures at the surface of the irradiated AuNSs, blue right axis of Fig. 4a, reveal that the temperature increases with  $\sim 325$  K at a power of 375 mW. The top panel of Fig. 4a shows representative confocal images of 633 nm

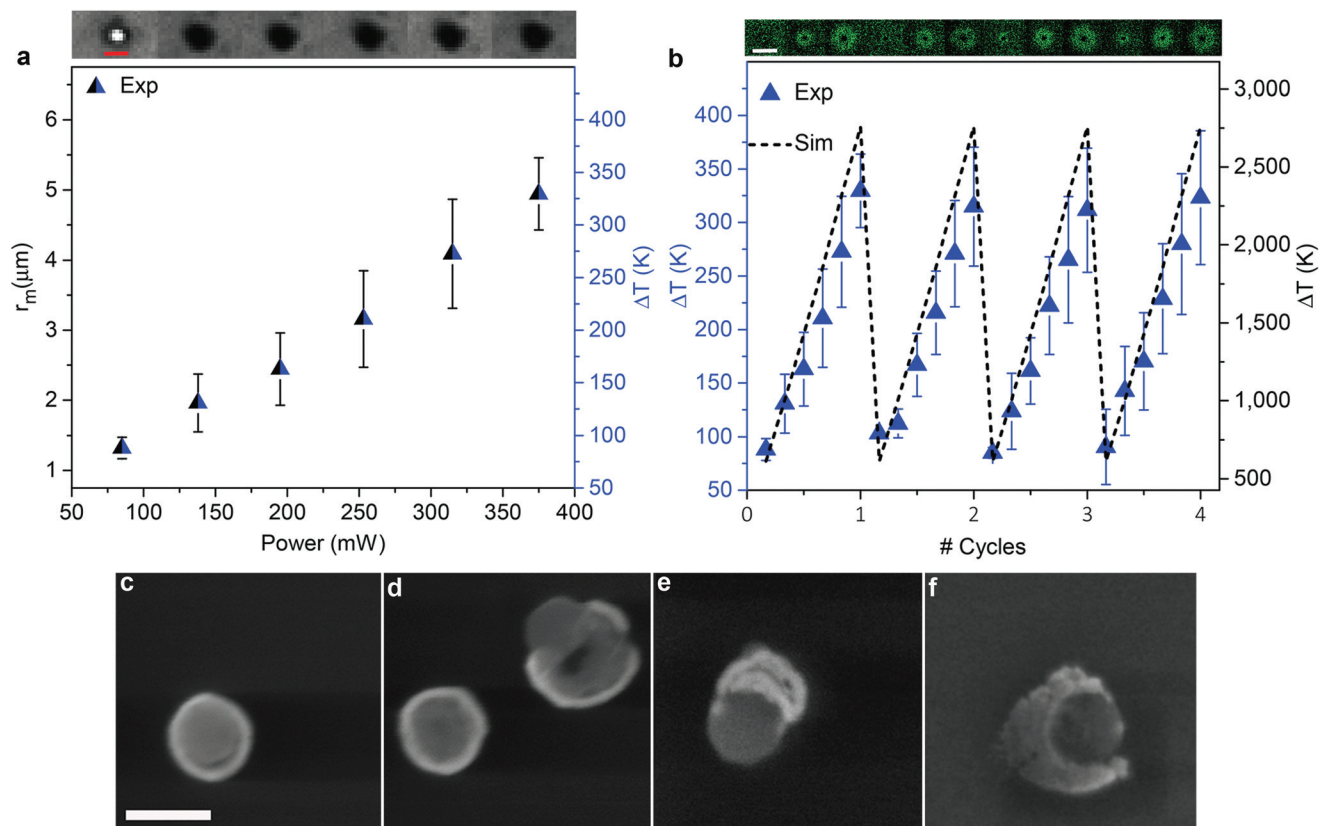


**Fig. 4** Quantification of heating and thermal stability of individual irradiated gold nanoshells (AuNSs). (a) Symbols show the experimentally measured melted radius (left axis) and corresponding surface temperature increase (right axis) for individual irradiated AuNSs with diameters of 150 nm as a function of laser power at the sample. The upper panel shows corresponding reflection images of an irradiated AuNS using 633 nm laser light, the red scale bar is 1  $\mu\text{m}$ . (b) Symbols show the experimentally determined temperatures (left axis) for individual AuNSs during repeated heating cycles, each cycle with laser powers as in (a). Each data point in (a) and (b) denotes measurements on at least  $n = 7$  different nanoparticles and the error bars denote one standard deviation. The dashed line (corresponding to units on the right axis) shows the FEM calculated temperature increase as a function of laser power for a AuNS. The upper panel displays corresponding confocal images of the partitioning of the phase-sensitive fluorophores. The white scale bar is 10  $\mu\text{m}$ . (c,d,e,f) Scanning electron microscopy images of AuNSs, the scale bar is 150 nm and is valid for all images. (c) An intact non-irradiated AuNS. (d) An intact non-irradiated AuNS (left) and a damaged irradiated AuNS (right). (e,f) Two more representative examples of irradiated and damaged AuNSs. The irradiation power of the NIR laser in (d,e,f) was  $P = 138$  mW at the sample. This laser power was chosen because it was the lowest laser power at which structural changes in the reflection images (top panels in (a)) were observed. The irradiation time was  $\sim 1$  s.

light reflected from the particle. The reflection image from a AuNS changes dramatically between the lowest laser power of 85 mW (center is bright) and the second laser power of 138 mW (center is black). This significant change in the backscattered signal indicates that the structure of a AuNS changes upon heating with concomitant aberration in the plasmonic properties at laser powers between 85 mW and 138 mW.

FEM simulations for AuNSs are shown in Fig. 4b with dashed lines and the corresponding numbers are given on the right axis (each cycle with laser powers as in Fig. 4a). For the AuNSs there is a large discrepancy, a factor of  $\sim 7$ , between the measured surface temperatures (Fig. 4b blue left axis) and the theoretical prediction (Fig. 4b black right axis). This discrepancy, in combination with the changed reflection images of irradiated AuNSs, indicates that AuNSs irreversibly change properties upon irradiation. Fragmentation or deformation of

nanoparticles upon photothermal heating, both by CW and pulsed irradiation, has previously been reported,<sup>39–41</sup> hence, it is likely that also the AuNSs undergo structural changes upon extensive heating.

To directly see the influence of irradiation on the structure of individual AuNSs we imaged the particles by scanning electron microscopy (SEM). Within the same sample, some AuNSs were irradiated with a 1064 nm NIR laser at  $P = 138$  mW (the lowest laser power causing a change of the AuNS's scattering properties) and others were not irradiated. Representative SEM images are shown in Fig. 4c–f, where Fig. 4c shows a non-irradiated AuNS, Fig. 4d a non-irradiated (left) and an irradiated (right) AuNS, and Fig. 4e and f show two additional examples of irradiated AuNSs. Upon NIR irradiation with  $P \sim 138$  mW, corresponding to temperatures exceeding  $\sim 100$  °C, the AuNSs significantly change appearance, thus indicating irreversible morphological changes.

When comparing the plasmonic heating of individual PtNPs directly to individual AuNSs irradiated by the same laser power and NIR wavelength, the PtNPs achieve significantly higher temperatures than AuNSs despite the higher absorption cross section of the AuNSs. This is explained by the fact that AuNSs undergo a structural degradation of the core-shell nanostructure when the temperature increase (from room temperature) exceeds  $\sim 100$  °C. The fact that AuNSs change structure upon heating to temperatures above  $\sim 100$  °C may be due to the difference in thermal expansion coefficients of the silica core and gold shell. For cancer therapies in living organisms, the desired temperatures are on the order of 40–50 °C, and at these relatively low temperature increases, the AuNSs appear stable.

In contrast to the AuNSs, the PtNPs exhibit an extreme thermal stability, even when heated to 700 °C there are no indications of structural changes. This is consistent with previous studies using electron microscopy showing that 8 nm PtNPs gradually start to exhibit surface melting when heated in an oven to around 600 °C.<sup>42</sup> Similar results have been obtained for 2 nm PtNPs on a graphene support which led to a complete melting of the Pt particle at 1400 °C.<sup>43</sup> Gold nanorods change shape at significantly lower temperatures<sup>40,44</sup> and spherical gold nanoparticles have been observed to fragment due to overheating by CW irradiation.<sup>39</sup> Pyramid-shaped dendritic platinum-copper alloy ( $\sim 100$  nm)<sup>45</sup> and trifolium-like Pt-PVP (16 nm)<sup>46</sup> nanoparticles have also been proposed for photothermal therapy. These dendritic pyramids and trifolium-like particles are, however, likely not as photo-stable as spherical PtNPs due to re-structuring of the complex branching structure of these nanoparticles.

### 3.4 Bulk photothermal efficiency

For many applications, for instance cancer therapy, the plasmonic particles are administered at a relatively large concentration and it is relevant to elucidate their collective plasmonic properties. Therefore, and because bulk experiments are commonly used in literature to characterize plasmonic particles,<sup>47–50</sup> we evaluated the performance of PtNPs and AuNSs in bulk experiments. This analysis was performed for Pt50 and Pt70, however, not for Pt30 as the heating of Pt30 was too small to be detectable.

Fig. 5a shows two consecutive cycles of first irradiating a cuvette containing Pt50, Pt70, AuNSs or pure water with a 1064 nm NIR laser for 30 minutes and then turning off the laser and letting the sample cool for 20 minutes. After  $\sim 20$  minutes of irradiation the temperature increase reached a steady state value,  $\Delta T_{\max}$ . The concentrations of the particles were such that the optical density,  $\lambda_L$ , of all samples, apart from the control sample with pure water, were matched to a value of  $\lambda_L = 0.14$ ; this is a standard way to compare light to heat conversion efficiency of nanoparticles of different material, shapes, and sizes.<sup>51,52</sup> The solutions containing PtNPs reached significantly higher temperatures than the solutions containing AuNSs, even at these modest temperature elevations where the AuNSs supposedly do not restructure.

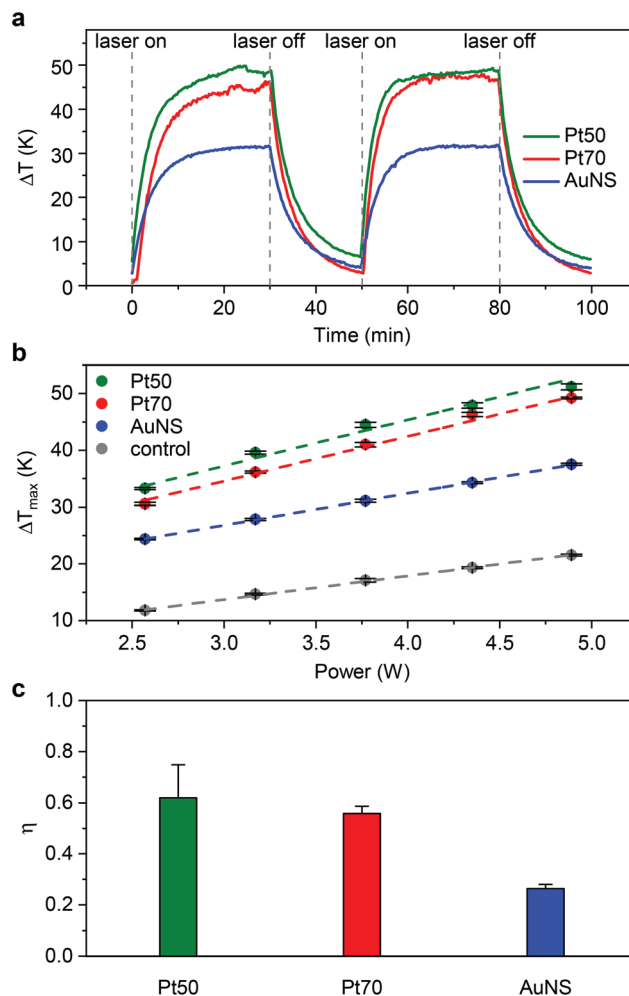


**Fig. 5** Heating of irradiated nanoparticle bulk solutions with matched optical densities. (a) Temperature increase as a function of time during two cycles of 30 minutes irradiation of nanoparticles followed by 20 minutes without laser for 50 nm PtNPs (green), 70 nm PtNPs (red), and 150 nm AuNSs (blue). The gray line is from a control experiment with Millipore water alone (no particles). The sampling rate is 4 per minute and the vertical dashed line indicates where the laser is switched on/off. The laser power for this data is  $P = 4.32$  W at the sample. The temperature increase,  $\Delta T$ , reaches a steady state value,  $\Delta T_{\max}$ , after  $\sim 20$  minutes of irradiation. (b)  $\Delta T_{\max}$  as a function of laser power. The error bars (nearly invisible) denote one standard deviation over 2.5 minutes with a sampling rate of 4 per minute. The dashed lines are linear fits to the data points, same color code as in (a). (c) Photothermal transduction efficiency,  $\eta$ , calculated as described in the ESI,<sup>†</sup> same color code as in (a),  $n = 3$  and error bars represent one standard deviation.

One can alternatively compare solutions with same mass density (see Fig. S4<sup>†</sup>). At the same mass density Pt50 and Pt70 solutions reached nearly the same  $\Delta T_{\max}$ , which was somewhat lower than for the mass density matched AuNS solution. Worth noticing is that upon density matching, the number of Pt50 ( $3.4 \times 10^{10}$  ml<sup>-1</sup>) is much larger than the number of Pt70 ( $1.2 \times 10^{10}$  ml<sup>-1</sup>), thus explaining that the Pt50 and Pt70 solutions reach the same temperature.



To compare how efficiently the different nanoparticles convert light to heat we also measured their photothermal transduction efficiency,<sup>47</sup>  $\eta$ :

$$\eta = \frac{hA(\Delta T_{\max}) - Q_0}{P(1 - 10^{-4t})} \quad (2)$$

Here  $h$  is the heat transfer coefficient,  $A$  is the sample chamber surface area,  $Q_0$  is the energy input from the solvent and the sample chamber without nanoparticles, and  $P$  is the laser power. The derivation of eqn (2) and details on the calculation of  $\eta$  from the experimental observables are given in the ESI.† From the control experiment with pure water we obtained  $Q_0$ . The photothermal transduction efficiencies,  $\eta$ , for Pt50, Pt70, and AuNSs are  $62\% \pm 13\%$ ,  $56\% \pm 3\%$ , and  $39\% \pm 2\%$ , respectively, as shown in Fig. 5c. The value of  $\eta$  for AuNSs is in agreement with the value calculated in Ayala-Orozco *et al.*<sup>13</sup> Hence, using  $\eta$  as a measure, Pt50 and Pt70 are more efficient heat transducers than the AuNSs.

### 3.5 Platinum nanoparticle toxicity

The potential of nanoparticles for *in vivo* usage ultimately relies on their toxicity to cells. To assess the toxicity of the investigated PtNPs on living cells we exposed human SK-OV-3 ovarian cancer cells to PtNPs for 24 hours at varying Pt mass concentrations up to  $50 \mu\text{g ml}^{-1}$ . We investigated the effects of

PtNP exposure on oxidative stress and cell death by flow cytometry (see Fig. 6). We observed no changes in neither cellular oxidative stress (Fig. 6a) nor apoptotic or necrotic cell death (Fig. 6b) for SK-OV-3 cells after 24 hours exposure to 30 nm, 50 nm or 70 nm PtNPs ( $0\text{--}50 \mu\text{g ml}^{-1}$ ) by analysis of variance (ANOVA) and following *post-hoc* tests. These results are consistent with the literature investigating the effect of platinum nanoparticles in silicone breast implants.<sup>53</sup> Using forward and side scattered light in flow cytometry we also examined the cell size and nanoparticle uptake for the same experiments (see Fig. S5†). Using the forward scattered light we did not observe any change in cell size with increasing PtNP concentrations (see Fig. S5†). However, we did observe a significant increase in the side scattered light, picked up at an angle of  $90^\circ$  relative to the propagation of the laser beam, from cells exposed to  $50 \mu\text{g ml}^{-1}$  of 70 nm PtNPs ( $P < 0.0001$  compared to  $0 \mu\text{g ml}^{-1}$  and  $P < 0.05$  compared to  $10 \mu\text{g ml}^{-1}$ ). Side scattered light has previously been successfully used to detect small relative differences in cellular uptake of metallic nanoparticles.<sup>54</sup> The side scattered light as a function of exposure for 30 nm, 50 nm, and 70 nm PtNPs is shown in Fig. S5† and indicates a cellular uptake that increases with particle size and concentration.

Pt-containing nanoparticles have previously been shown to exhibit anti-oxidant behavior by scavenging oxygen radicals.<sup>55</sup> Also, Au nanorods coated with Pt showed substantial reduction

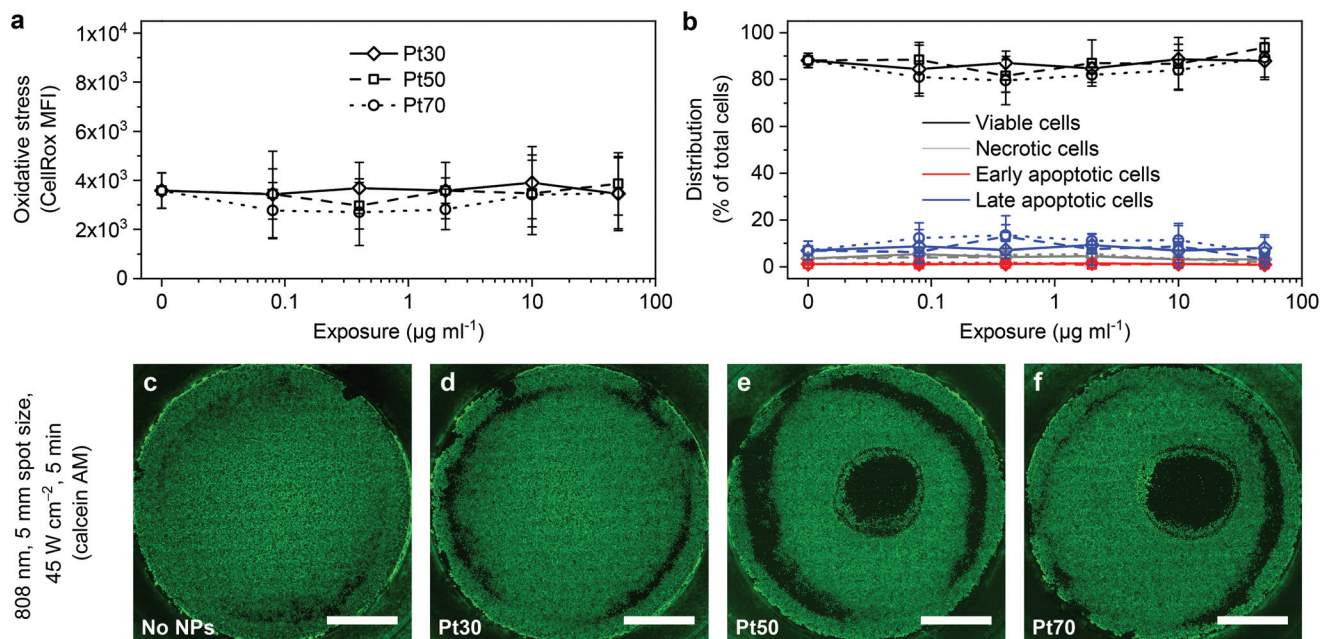


**Fig. 6** Toxicity studies and photothermal therapy of human SK-OV-3 ovarian cancer cells. (a) Cellular oxidative stress as a function of exposure concentration for a human SK-OV-3 ovarian cancer cell line exposed to platinum nanoparticles (without irradiation). The graph shows flow cytometry analysis of SK-OV-3 cells after 24 hours of exposure to 30 nm PtNPs (diamond symbols connected by solid lines), 50 nm PtNPs (squares connected by dashed line), and 70 nm PtNPs (circles connected by dotted lines). MFI = median fluorescent intensity. (b) Cell death as a function of exposure concentration for SK-OV-3 cells after 24 hours of exposure to 30 nm PtNPs (diamond symbols connected by solid lines), 50 nm PtNPs (squares connected by dashed line), or 70 nm PtNPs (circles connected by dotted lines). Error bars represent one standard deviation,  $n = 3$ . (c–f) Photothermal therapy of human SK-OV-3 ovarian cancer cells. Images of cancer cells stained with calcein AM 24 h after photothermal treatment. During treatment, the cells were exposed to  $50 \mu\text{g ml}^{-1}$  PtNPs of varying sizes and laser irradiated by a 5 mm flat-top 808 nm beam with laser power  $45 \text{ W cm}^{-2}$  for 5 minutes. (c) is a control without particles, (d) contains irradiated 30 nm PtNPs, (e) contains irradiated 50 nm PtNPs, and (f) contains irradiated 70 nm PtNPs. Scale bar = 5 mm.

in the production of reactive oxygen species during photothermal therapy of cancer cells, but with the same cancer killing efficiency than uncoated Au nanorods.<sup>56</sup> Therefore, it is expected that PtNPs will cause less unwanted negative local effects on healthy neighboring cells due to photothermal therapy mediated ROS production compared with, *e.g.*, gold nanoparticles.

### 3.6 Platinum nanoparticle based photothermal cancer therapy

The non-irradiated PtNPs were non-toxic for SK-OV-3 cells, however, we also explored the PtNPs' potential for photothermal cancer therapy. For this the SK-OV-3 cancer cells were cultivated in glass-bottom wells and exposed to no PtNPs (control) or to 30 nm, 50 nm, or 70 nm PtNPs for 24 hours prior to the laser treatment. The cells were thoroughly rinsed before laser treatment to remove any excess or loosely bound PtNPs. A circular area, diameter  $\sim 5$  mm, of the cell-coated well was then irradiated by a flat-top 808 nm beam using a laser intensity of  $45 \text{ W cm}^{-2}$  for 5 minutes. After photothermal therapy the cells were returned to normal cell culture conditions for 24 hours before we performed a standard calcein AM viability staining and with subsequent fluorescent imaging, the results are shown in Fig. 6c–f.

Without exposure to PtNPs, the cells were not affected by the laser treatment (see example in Fig. 6c). The outer dark ring with a diameter of  $\sim 1.5$  cm visible in Fig. 6 is apparent in all images and arises from a lower adhesion of cells close to the rim of the well. Likewise, cancer cells exposed to 30 nm PtNPs and laser treated were not observably affected (Fig. 6d). This is consistent with the observation that individual 30 nm PtNPs do not heat upon irradiation, however, it is not trivial since particles are known to cluster tightly after internalization in cells, which can change their plasmonic properties.<sup>54,57</sup> Cancer cells exposed to 50 nm or 70 nm PtNPs were convincingly affected by the laser treatment as this produced a clear circular area (roughly 5 mm in diameter, same diameter as the laser beam) with no living cells (Fig. 6e and f). There is no apparent difference between the efficiency of Pt50 and Pt70 in photothermal treatment of cancer cells and these results demonstrate that NIR photothermal therapy based on 50 nm or 70 nm PtNPs can successfully kill human cancer cells.

## 4 Conclusion

In summary, we find platinum nanoparticles capable of reaching temperatures as high as  $700^\circ\text{C}$  while maintaining structural integrity, thus being exceptionally thermally stable compared to other metallic nanoparticles. One advantage of the PtNPs investigated here is their size. The smaller size of the plasmonic PtNPs (50–70 nm), compared to the larger NIR light resonant AuNSs (150 nm), is closer to the optimal particle size for cellular uptake which, for gold nanoparticles, is found to be  $\sim 50$  nm.<sup>12,58</sup> Also, the scattering cross section of AuNSs at NIR wavelengths is significantly higher than the scattering

cross section of PtNPs, hence, NIR light will penetrate deeper into material, *e.g.*, tumor tissue, loaded with PtNPs than with AuNSs. Besides photothermal cancer therapy, laser activated PtNPs have a broad range of possible applications, for instance in combination with targeted drug delivery,<sup>15–17</sup> where the metallic nanoparticle upon irradiation releases (part of) its coating. Or for hot-nanoparticle based fusion of selected cells or vesicles.<sup>18,19</sup> Also, for photo-induced catalysis in bio- and medical applications, the extreme photo-thermal capabilities and stability of platinum is an advantage.<sup>22,59,60</sup> The plasmonic properties of PtNPs and their low toxicity, in connection with the commercial availability of high quality PtNPs, makes the future bright for utilizing these exceptional particles for hot bio-engineering purposes.

## Conflicts of interest

There are no conflicts to declare.

## Acknowledgements

The authors thank Berit Wenzell, CEN, DTU for support with the SEM microscopy and acknowledge financial support from the Novo Nordisk Foundation, synergy grant NNF14OC0011361, from the Danish Council for Independent Research (DFF) grant number 4181-00196A, and from the Danish National Research Foundation DNR116.

## References

- 1 X. Huang, P. K. Jain, I. H. El-Sayed and M. A. El-Sayed, *Lasers Med. Sci.*, 2008, **23**, 217–228.
- 2 C. Burda, X. Chen, R. Narayanan and M. A. El-Sayed, *Chem. Rev.*, 2005, **105**, 1025–1102.
- 3 G. Baffou, R. Quidant and C. Girard, *Appl. Phys. Lett.*, 2009, **94**, 153109.
- 4 M. L. Brongersma, N. J. Halas and P. Nordlander, *Nat. Nanotechnol.*, 2015, **10**, 25–34.
- 5 S. H. Yun and S. J. J. Kwok, *Nat. Biomed. Eng.*, 2017, **1**, 0008.
- 6 C. Loo, A. Lowery, N. J. Halas, J. West and R. Drezek, *Nano Lett.*, 2005, **5**, 709–711.
- 7 S. Lal, S. E. Clare and N. J. Halas, *Acc. Chem. Res.*, 2008, **41**, 1842–1851.
- 8 R. Bardhan, W. Chen, C. Perez-Torres, M. Bartels, R. M. Huschka, L. L. Zhao, E. Morosan, R. G. Pautler, A. Joshi and N. J. Halas, *Adv. Funct. Mater.*, 2009, **19**, 3901–3909.
- 9 J. T. Jørgensen, K. Norregaard, P. Tian, P. M. Bendix, A. Kjaer and L. B. Oddershede, *Sci. Rep.*, 2016, **6**, 30076.
- 10 D. Jaque, L. Martínez Maestro, B. del Rosal, P. Haro-Gonzalez, A. Benayas, J. L. Plaza, E. Martín Rodríguez and J. García Solé, *Nanoscale*, 2014, **6**, 9494–9530.

- 11 H. Maeda, J. Wu, T. Sawa, Y. Matsumura and K. Hori, *J. Controlled Release*, 2000, **65**, 271–284.
- 12 B. D. Chithrani, A. A. Ghazani and W. C. W. Chan, *Nano Lett.*, 2006, **6**, 662–668.
- 13 C. Ayala-Orozco, C. Urban, M. W. Knight, A. S. Urban, O. Neumann, S. W. Bishnoi, S. Mukherjee, A. M. Goodman, H. Charron, T. Mitchell, M. Shea, R. Roy, S. Nanda, R. Schiff, N. J. Halas and A. Joshi, *ACS Nano*, 2014, **8**, 6372–6381.
- 14 R. Bardhan, S. Lal, A. Joshi and N. J. Halas, *Acc. Chem. Res.*, 2011, **44**, 936–946.
- 15 R. Huschka, J. Zuloaga, M. W. Knight, L. V. Brown, P. Nordlander and N. J. Halas, *J. Am. Chem. Soc.*, 2011, **133**, 12247–12255.
- 16 R. Huschka, A. Barhoumi, Q. Liu, J. A. Roth, L. Ji and N. J. Halas, *ACS Nano*, 2012, **6**, 7681–7691.
- 17 X. Huang, A. Pallaoro, G. B. Braun, D. P. Morales, M. O. Ogunyankin, J. Zasadzinski and N. O. Reich, *Nano Lett.*, 2014, **14**, 2046–2051.
- 18 A. Rorvig-Lund, A. Bahadori, S. Semsey, P. M. Bendix and L. B. Oddershede, *Nano Lett.*, 2015, **15**, 4183–4188.
- 19 A. Bahadori, L. B. Oddershede and P. M. Bendix, *Nano Res.*, 2017, **10**, 2034–2045.
- 20 E. Reddington, A. Sapienza, B. Gurau, R. Viswanathen, S. Sarangapani, E. Smotkin and T. Mallouk, *Science*, 1998, **280**, 1735–1737.
- 21 R. Narayanan and M. El-Sayed, *Nano Lett.*, 2004, **4**, 1343–1348.
- 22 S. Linic, U. Aslam, C. Boerigter and M. Morabito, *Nat. Mater.*, 2015, **14**, 567–576.
- 23 K. Svoboda and S. M. Block, *Annu. Rev. Biophys. Biomol. Struct.*, 1994, **23**, 247–285.
- 24 P. M. Hansen, V. K. Bhatia, N. Harrit and L. Oddershede, *Nano Lett.*, 2005, **5**, 1937–1942.
- 25 A. Samadi, P. M. Bendix and L. B. Oddershede, *Nanoscale*, 2017, **9**, 18449–18455.
- 26 J. Li, Y. Huang, Y. Ding, Z. Yang, S. Li, F. Fan, W. Zhang, Z. Zhou, D. Wu, Z. Want and Z. Tian, *Nature*, 2010, **464**, 392–395.
- 27 P. R. West, S. Ishii, G. V. Naik, N. K. Emani, V. M. Shalaev and A. Boltasseva, *Laser Photonics Rev.*, 2010, **4**, 795–808.
- 28 G. V. Naik, V. M. Shalaev and A. Boltasseva, *Adv. Mater.*, 2013, **25**, 3264–3294.
- 29 H. Ma, P. Tian, J. Pello, P. M. Bendix and L. B. Oddershede, *Nano Lett.*, 2014, **14**, 612–619.
- 30 A. O. Govorov, W. Zhang, T. Skeini, H. Richardson, J. Lee and N. A. Kotov, *Nanoscale Res. Lett.*, 2006, **1**, 84–90.
- 31 X. Chen, Y. Chen, M. Yan and M. Qiu, *ACS Nano*, 2012, **6**, 2550–2557.
- 32 G. Baffou, R. Quidant and F. J. Garcia de Abajo, *ACS Nano*, 2010, **4**, 709–716.
- 33 P. M. Bendix, S. N. Reihani and L. B. Oddershede, *ACS Nano*, 2010, **4**, 2256–2262.
- 34 A. C. Richardson, N. Reihani and L. B. Oddershede, *Proc. SPIE*, 2006, **6326**, 632628.
- 35 M. Manikandan, N. Hasan and H.-F. Wu, *Biomaterials*, 2013, **34**, 5833–5842.
- 36 S. Merabia, S. Shenogin, L. Joly, P. Keblinski and J. L. Barrat, *Proc. Natl. Acad. Sci. U. S. A.*, 2009, **106**, 15113–15118.
- 37 K. Sasikumar, Z. Liang, D. G. Cahill and P. Keblinski, *J. Chem. Phys.*, 2014, **140**, 234506.
- 38 K. Setoura, Y. Okada, D. Werner and S. Hashimoto, *ACS Nano*, 2013, **7**, 7874–7885.
- 39 K. Setoura, Y. Okada and S. Hashimoto, *Phys. Chem. Chem. Phys.*, 2014, **16**, 26938–26945.
- 40 H. Y. Ma, P. M. Bendix and L. B. Oddershede, *Nano Lett.*, 2012, **12**, 3954–3960.
- 41 W. Albrecht, T. S. Deng, B. Goris, M. A. van Huis, S. Bals and A. van Blaaderen, *Nano Lett.*, 2016, **16**, 1818–1825.
- 42 Z. L. Wang, J. M. Petroski, T. C. Green and M. A. El-Sayed, *J. Phys. Chem. B*, 1998, **102**, 6145–6151.
- 43 M. S. Moldovan, H. Bulou, Y. J. Dappe, I. Janowska, D. Bégin, C. Pham-Huu and O. Ersen, *J. Phys. Chem. C*, 2012, **116**, 9274–9282.
- 44 C. Ungureanu, R. Kroes, W. Petersen, T. A. M. Groothuis, F. Ungureanu, H. Janssen, F. W. B. van Leeuwen, R. P. H. Kooyman, S. Manohar and T. G. van Leeuwen, *Nano Lett.*, 2011, **11**, 1887–1894.
- 45 Z. Zhou, K. Hu, R. Ma, Y. Yan, B. Ni, Y. Zhang, L. Wen, Q. Zhang and Y. Cheng, *Adv. Funct. Mater.*, 2016, **26**, 5971–5978.
- 46 C. Wang, X. Cai, J. Zhang, X. Wang, Y. Wang, H. Ge, W. Yan, Q. Huang, J. Xiao, Q. Zhang and Y. Cheng, *Small*, 2015, **11**, 2080–2086.
- 47 D. K. Roper, W. Ahn and M. Hoepfner, *J. Phys. Chem. C*, 2007, **111**, 3636–3641.
- 48 J. R. Cole, N. A. Mirin, M. W. Knight, G. P. Goodrich and N. J. Halas, *J. Phys. Chem. C*, 2009, **113**, 12090–12094.
- 49 H. Chen, L. Shao, T. Ming, Z. Sun, C. Zhao, B. Yang and J. Wang, *Small*, 2010, **6**, 2272–2280.
- 50 B. Jang, Y. S. Kim and Y. Choi, *Small*, 2011, **7**, 265–270.
- 51 V. P. Pattani and J. W. Tunnell, *Lasers Surg. Med.*, 2012, **44**, 675–684.
- 52 R. Bardhan, N. K. Grady, J. R. Cole, A. Joshi and N. J. Halas, *ACS Nano*, 2009, **3**, 744–752.
- 53 M. A. Brook, *Biomaterials*, 2006, **27**, 3274–3286.
- 54 H. Klingberg, L. B. Oddershede, K. Loeschner, E. H. Larsen, S. Loft and P. Møller, *Toxicol. Res.*, 2015, **4**, 655–666.
- 55 M. Kajita, K. Hikosaka, M. Iitsuka, A. Kanayama, N. Toshima and Y. Miyamoto, *Free Radical Res.*, 2007, **41**, 615–626.
- 56 M. Aioub, S. R. Panikkanvalappil and M. A. El-Sayed, *ACS Nano*, 2017, **11**, 579–586.
- 57 V. P. Zharov, J. W. Kim, D. T. Curiel and M. Everts, *Nanomedicine*, 2005, **1**, 326–345.
- 58 L. Shang, K. Nienhaus and G. U. Nienhaus, *J. Nanobiotechnol.*, 2014, **12**, 5.
- 59 S. S. Bhoware, K. Y. Kim, J. A. Kim, Q. Wu and J. Kim, *J. Phys. Chem. C*, 2011, **115**, 2553–2557.
- 60 L. Liu, P. Miao, Y. Y. Xu, Z. P. Tian, Z. G. Zou and G. X. Li, *J. Photochem. Photobiol., B*, 2010, **98**, 207–210.